

Cloud Motion Estimation for Short Term Solar Energy Prediction

Hao Huang ^{#1}, Jin Xu ^{#2}, Zhenzhou Peng ^{#3}, Shinjae Yoo ^{*4}, Dantong Yu ^{*5}, Dong Huang ^{*6}, Hong Qin ^{#7}

[#]*Stony Brook University*

100 Nicolls Road, Stony Brook, NY 11794

¹haohuang@cs.stonybrook.edu

²xujinhust@gmail.com

³mikegrup@gmail.com

⁷qin@cs.stonybrook.edu

^{*}*Brookhaven National Laboratory*

50 Bell Avenue, Upton, NY 11973

⁴sjyoo@bnl.gov

⁵dyu@bnl.gov

⁶dhuang@bnl.gov

Abstract—Variability of solar energy is the most significant issue for integrating solar energy into the power Grid. There are pressing demands to develop methods to accurately estimate cloud motion that directly affects the stability of solar power output and benefit of adding this type of power into the Grid. In this paper, we propose a solar prediction system that can detect cloud movements from the TSI (total sky imager) images, and then estimating the future cloud position over solar panels and subsequent solar irradiance fluctuations incurred by cloud transients. The experiment studies show that our proposed approach significantly improves the quality of cloud motion estimation within a time window (up to a few minutes) that is sufficient for grid operators to take actions to mitigate the solar power volatility.

I. INTRODUCTION

Due to the rising cost and severe impacts to environment associated with fossil fuel, alternative or renewable energy solutions gained more attraction in the past several decades, including photovoltaic also known as solar energy, wind, rain, tides, and so on. Solar energy is one of the most promising solutions due to the following facts: 1) The equipment can be deployed on the rooftop of residential and industry buildings and virtually no restriction on installation locations, 2) it is noise-free, 3) it requires less maintenance, and has a longer lifetime because of its simple involving no moving parts, and 4) it is economically viable because the price of solar panel keeps decreasing compared to the equipment required by other forms of renewable energy sources.

Exploiting solar energy is highly challenging because it cannot be used as an on-demand stable power source and has fundamentally constrained production hours. Variability in solar source is the biggest hurdle in integrating solar energy into the national Grid. Furthermore, the cloud variability changes significantly demands high standards on capacity forecasting. Various solutions, such as backup generators, batteries, power trade and exchange were proposed to mitigate beforehand the

undesired random behavior. However these solutions must be built upon the accurate prediction of photovoltaic (PV) output in particular for the time period from a few seconds to minutes that is long enough to wake up the backup substitute sources.

Cloud motion is the primary reason for photovoltaic (PV) output fluctuation. In essence, short-term PV output prediction can be simplified as cloud motion estimation. Cloud lifetime varies from ten minutes (small cumulus) to a few days (some types of stratus) depending on cloud type and atmospheric conditions. A typical cumulus cloud whose lifetime usually last only a few minutes is the most important for solar farm scale forecasting. Local weather forecast provides some global cloud coverage information on a daily basis, but is certainly insufficient for our prediction requirement which has small time granularities and spatial resolutions. High resolution cloud-resolving radar can track cloud location, height and motions, but is prohibitively expensive and hence also not practical for solar installations.

In this research, our goal is to provide **cost-effective cloud motion prediction models** that require no expensive equip-

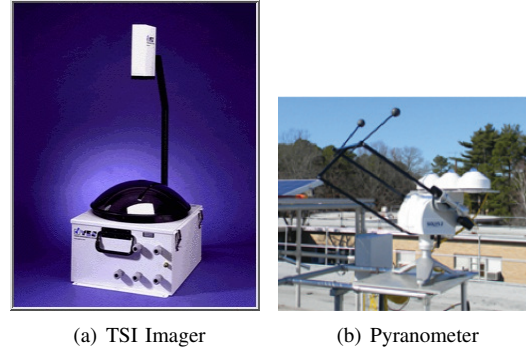


Fig. 1.

ment while meeting the accuracy and performance requirements. We address the variability problem of cloud motion with Total Sky Imager (TSI) [14], a cost-effective solution to take hemispheric images of the whole visible sky (Figure 1(a)). We detect cloud motion vectors between TSI images and use them to estimate future cloud motion over the location where solar panels reside. Note that TSI result alone does not predict solar radiation level or PV panel output directly. Instead, the prediction result of cloud motion can be used to calculate solar radiation level or PV output level with the predicted location of cloud, Sun position, the timestamps and locations of TSI. A second device, a pyranometer installed at the same location as the TSI, is used to monitor the level of solar irradiance on the ground. This produces a continuous data stream of the solar irradiance in a time series format. Its numerical correlation with the cloud motion from the TSI images is captured by our proposed model for predicting the solar radiation values on site. These two devices together offer us a complete yet highly economic input setup for our prediction objectives.

This paper addresses several challenges which are unique to the cloud motion estimation techniques: 1) The proposed prediction algorithm has to be real-time, and requires no more than five seconds to obtain the result for predicting what will happen in 10 seconds to a few minutes. Backup devices to mitigate solar power volatility can be scheduled and activated within this prediction window. Longer prediction (hourly and daily) that requires different atmospheric data is not the focus of this paper. 2) Cloud shape changes continuously over time. Even minor shape change can cause the instability to cloud motion tracking. 3) Cloud has multiple layers, each of which has different velocities and/or directions. The high altitude cloud appears and disappears in the 2D TSI images because of velocity difference. This often confuses with the cloud shape changes. 4) TSI loses some information due to the holding arm, shadow band, and boarder of circular images (Figure 2), and it is difficult to track cloud motions around these area. 5) Clouds' direct influence on solar irradiance is reflected in a complex way through the TSI images color patterns and textures. We will select the most significant pattern of the TSI image for our radiation prediction model.

This paper proposes novel cloud estimation methods with the summarized contributions listed below:

- 1) The novelty of our methodology is that we use almost solely TSI images as input, so our subsequent analysis requires no other meteorological input (eg. humidity, wind velocity). Moreover our work focus on predicting cloud motion that occur within short term and directly over the solar panels. Hence it is microscopic and structurally different from most of the existing mesoscale approaches [4], [5], [19], [20], [21] which target a larger scale and longer-term prediction by making use of physical atmospheric conditions as crucial input. A most recent work similar to ours is [26]. Their model will be used as a baseline for comparison and its technical limitations will be discussed later in this paper.
- 2) We propose to use fast cross correlation algorithm for ef-

fective and real-time cloud motion tracking (Section IV). In particular, the Adopted Fast Cross Correlation is a combination of the fastest method (Phase Correlation) and more robust and error tolerant yet slower method (Cross Correlation). It satisfies our real-time speed requirement and is sufficient for the precision of cloud motion tracking in the mean time.

- 3) We propose the following cloud tracking improvements over the generic cross correlation based algorithms which are customized for our TSI image processing needs and solar radiation prediction testings (Section V):
 - a) **Gap filling** We propose to use local mean filling and estimated image filling for gaps in all of the TSI images. As a result, abnormal cloud tracking were significantly reduced and the accuracy of cloud tracking algorithm was improved.
 - b) **Cloud tracking model based on consecutive TSI images** A sequence of consecutive images (more than two) are used in our approach to take into account possible minor cloud shape changes and gaps in images. This approach is termed as “sequential motion vector prediction”, which in theory, should outperform those only consider two continuous time frames [26]. In our paper, significant cloud changes are not considered because they rarely happen within our chosen time window for prediction, i.e. between 10 seconds to 10 minutes [25].
 - c) **Wind-field** Wind-field is the three-dimensional spatial patterns of wind. This information can be utilized in resolving multi-layer cloud problems (lack of being considered in [26]), in particular, cloud tracking and cloud motion estimation. This layer recognition method has potential because it does not require the cloud base height detection using additional devices.

Our novel cloud motion estimation algorithms based on these improvements both on single layer and multi-layer cloud can be found in (Section VI).

- 4) Finally, we propose a **Linear Prediction model** for short term forecasting of solar irradiance levels and compare the model output with real-life TSI and pyranometer data. Our model has the crucial feature of expendability which is often lacking from physical and atmospherical motivated models. Our model can easily expand in the future to include more TSI details in terms of textures and cloud types as well as the number of parameters. In addition, longer TSI image sequences of previous samples are used in our model in order to improve the accuracy of our short term predictions. The algebraic structure of the solar irradiance prediction model also allows us to easily adapt to a larger variety of other data sources.

The systematic evaluation of our proposed algorithms and the linear solar irradiance forecasting model can be found in Section VIII. For the former, a total of 2880 sky images from four days with highly varied cloud conditions are chosen for a thorough study. The experiments confirm that our proposed

algorithms can significantly improve the accuracy of cloud tracking and motion detection over existing methods. For the solar irradiance prediction, we employ the 10-fold cross validation to evaluate our system's performance using the independent binary method in [26] as baseline for comparison. The experiments showed that our system can significantly reduce errors in predicting the real-time solar irradiance values.

II. BACKGROUND

The total sky imager (TSI) (Figure 1(a)) which is manufactured by Yankee Environmental Systems (YES) Inc., provides a series of continuous hemispheric full-color sky images. The sky images allow us to accurately compute and predict cloud coverage and solar radiation levels. Pyranometers (Figure 1(b)) monitor in real-time solar resource conditions and outputs the solar irradiance index value in the unit of Watts per square meter (W/m^2). Pyranometer sensors were installed at the same site for cross reference, and calibration. All field measurement output is recorded at time intervals as rapid as 1/minute (shown as a black line in Figure 13 in Section VIII).

Many techniques have been developed to detect object motion vectors. However, due to the unique properties of cloud image, only a few of them are actually appropriate for cloud motion detection. Arrays of similar partial cloud can generate multiple narrow extrema in the correlation surface, which could mislead SSDA (sequential similarity detection algorithm [7]), for instance. Since cloud often does not have a clear boundary, active contour models such as Snakes [8] are difficult to implement. Wavelets and other multi-resolution schemes [2], [9], [1], to some extent, are not suitable to TSI image because of the lower resolution of TSI especially near the boundary area, where ideal features are usually hard to identify. Local feature based methods [10], [11], [12], [13] are robust to deformable objects, but they require long CPU time to compute, therefore make it harder to meet the real-time applicability requirement.

Optical flow is the pattern of apparent motion of objects, surfaces, and edges in a visual scene caused by the relative motion within captured frames. Nowadays optical flow has been applied in estimating the object motion [3], [23], [24]. Our proposed algorithms are based on one of the classic methods for determining optical flow: maximizing normalized correlation on block-based image matching.

A most recent study with similar goals to our research is [26]. A few major drawbacks of this work are: 1) it applies the simple correlation-based method and fails to consider multi-layer clouds, which frequently occur in their studied sky area; 2) it uses only two most recent time frames to predict the cloud motion in the upcoming future frame. 3) We propose to use fast cross correlation to meet real-time requirements. 4) Our overall cloud motion estimation is much more sophisticated including a much refined gap filling method. 5) The binary model for cloud condition is much too crude for tagging various other types of weather condition and causes a great barrier to expand their model's applicability and capacity for more complex cloud patterns and the corresponding TSI data.

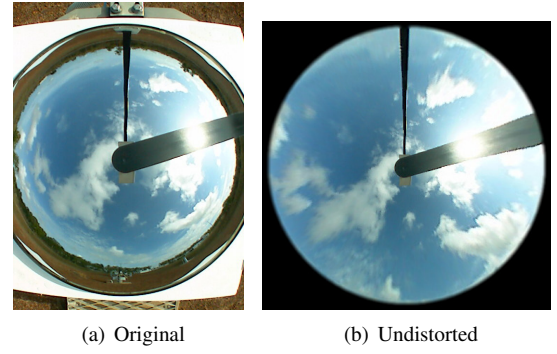


Fig. 2. TSI Image Undistortion

Targeting these existing problems, our paper introduce novel and practical techniques for both cloud motion estimation and solar irradiance prediction. In the case of solar irradiance prediction this is achieved by a Linear Prediction model using continuous values of both TSI and pyranometer inputs.

A general hierarchical framework for motion tracking is discussed in [15]. An early empirical study of five template matching algorithms in the presence of various image distortions [16] found that the cross correlation method provides the best performance in all image categories. Later in [4], Marcello et.al. surveyed region matching techniques and concluded that (normalized) cross correlation is one of the most favored choices for cloud motion detection. The main reason is that cross correlation method makes fewer requirements on the image sequence and has fewer parameters to be tuned by the user. It can be used “as is” to provide simple feature tracking. The choice of the correlation coefficient over alternative matching criteria such as the sum of absolute differences has also been justified by maximum-likelihood estimation [17].

Linear prediction model has been widely used in diverse areas ranging from optimization, control to speech processing, in particular, the aforementioned cloud motion prediction algorithm. Since its mathematical background is traced to the matrix linear algebra, linear prediction is suited well for the discrete time series that can be found in both input data streams (TSI images and Solar irradiance) to our model. Our model aims to deal with the volatile local weather conditions and therefore needs to use the input data with continuous value for accurate prediction quality to capture transient weather conditions. In contrast, the currently available model in [26] is binary and cannot deliver a comparable precision for solar irradiance prediction.

Due to its linear structure, our prediction model can be easily expanded to include more types of input data and make use of data from multiple past time steps. This is desirable especially for building more sophisticated models in future to utilize more features, such as texture information from TSI images, to meet various prediction requirements.

III. ALGORITHM FRAMEWORK

Before investigating all the key steps of our cloud estimation methods, we present a schematic overview of our proposed

algorithm in Figure III. The whole process consists of three stages: TSI image preprocessing, Cloud motion estimation and Solar radiation estimation.

The key step of TSI image preprocessing is mapping the original non-flat TSI image space into a flat one, so that the motion vectors can be detected with uniform/similar size. We call this step TSI image undistortion. Besides the undistortion, image center alignment and shadowband, camera-holding arm removal are also processed in the preprocessing step.

Cloud motion estimation is composed of two motion detection steps and two motion estimation steps. The reason of double detection and estimation is because of the requirement of filling missing information. Motion estimation quality will be affected by the missing information (holding arm, shadowband and outside of boundary area). To overcome this, we compute during the first round rough motion estimation to fill in missing information on the TSI image. Once we obtain the complete sky images, the second motion detection will be run and the second estimation based on the improved motion detection results produce more accurate sky predictions.

Finally, The output of cloud motion estimation will be used to estimate the solar irradiance level in a specific time range. We will build both deterministic and statistical modeling of cloud variation to characterize cloud transients and predict the associated intermittencies of solar generation. The proposed forecast model will identify the sophisticated correlation between cloud motion and the anticipated decrease or increase in power output at a specific centralized generating site.

IV. FAST AND EFFECTIVE MOTION VECTOR DETECTION

In this section, we describe the motion vector detection methods which meet real-time requirements and yet are effective enough. In [6], Huang et.al. already investigated two most popular motion vector detection approaches: Phase Correlation (PC) and Cross Correlation (CC), and discussed the advantages and disadvantages for both of them when used in cloud motion detection. Here we describe the fast cross correlation adopted in our research because of its speed and effectiveness.

Given a prior $N \times N$ sub-frame f , cross correlation method [6] looks for the most correlated current sub-frame g of the same block size from candidate search space $M \times M$ where $M > N$. However the cross correlation is mathematically similar to convolution, it is computationally expensive. Lewis [18] presented an algorithm for the fast normalized correlation calculation. Since the image can be normalized and the mean is zero, the numerator of cross correlation formula is a convolution of the image with the reversed feature $g'(-x, -y)$ where $g' = g - \bar{g}$ and can be computed using the following equation.

$$FFT^{-1}\{FFT(f')FFT^*(g')\} \quad (1)$$

Therefore the time complexity for the nominator is $O(M^2 \cdot \log M)$. For the denominator, Lewis used the technique of computing a definite sum from a precomputed running sum. Using two sum tables over the image function f and image energy f^2 , the sum tables are pre-computed integrals of f and

f^2 over the search image. So for a window of size $M \times M$, it can efficiently reduce the arithmetic operations from $M \times M$ to only three addition/subtraction operations per pixel once the sum tables are established. In other word, the construction of the tables requires approximately $O(M^2)$ operations, which is far less than the cost of computing the numerator and considerably less than $O(M^2 \cdot N^2)$ required to compute cross correlation at each pixel.

V. MOTION VECTOR REFINEMENTS

Although the real-time requirements of motion vector detection can be satisfied by our adopted fast cross correlation, the detected motion vectors still need significant improvements to be useful for accurate prediction. We summarize the challenges specific to cloud image processing and propose how to improve motion vector detection.

A. Challenges

We characterize cloud motion vector detection challenges into three categories:

- 1) **Missing Information** Figure 2(b) shows no sky information at the areas of holding arm, shadow band and outside of circle. The lack of sky information leads to no motion vector detected within and around these blank areas. Even worse, the detected motion vectors falsely align with the edges of the circle or the shadowband, an artifact caused by the contrast between these blank areas and other sky image areas. We call this phenomena as “*boundary effects*”.
- 2) **Minor Cloud Shape Changes** Although we assume no dramatical cloud shape changes in Section IV, minor and smooth changes of cloud shape may still occur within a short period of time, and lead to the problem that the motion vectors are deviated from the remain motion vectors. Note that this does not necessarily mean that the overall direction of cloud motion changes within such a short-time range (less than 10 minutes).
- 3) **Multi-layer Clouds** When there are two or more cloud layers, we can only observe the lowest layer in the view from the ground. The motion vectors around cloud boundary between two cloud layers are hard to detect. That results in abnormal motion vectors. It is a problem for not only the motion vector detection but also the subsequent cloud motion estimation.

These concerns will be addressed in the rest of this section.

B. Different Block Sizes

Our TSI image area is a circle but the motion vector detection algorithms use rectangular, which makes it difficult to detect cloud motion vector near the edge of images. If the block size is small, then we may get more motion vectors near the boundaries of TSI images. However, with the smaller block size, the detected motion vectors may not be as robust as the bigger block size. To resolve this problem, we use concurrently two different block sizes, the bigger block size for the center of an image and the smaller block size for pixels close to circle edge of an TSI image. With the proposed two block sizes, we

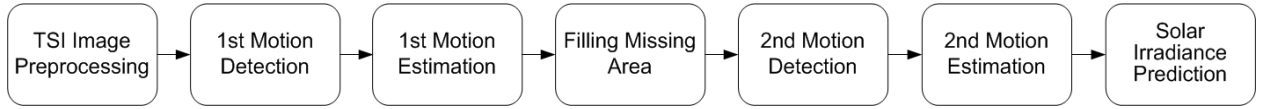


Fig. 3. Overall Cloud Motion Estimation Flow

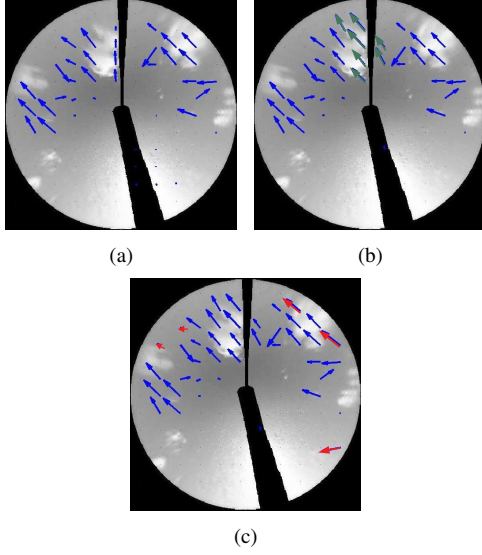


Fig. 4. Missing Information Refinement. Green arrows shows the improvements of local mean filling (b) and red arrows shows the improvements of two different block sizes (c). We reduce the number of motion vectors and increase the motion vector size to show them clearly

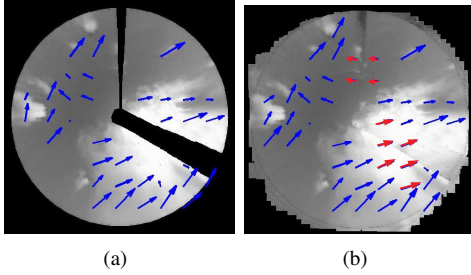


Fig. 5. Filling the missing information with the estimated images. (a) The motion vector detection after filling with the estimated image (b) found additional (red) motion vectors near the holding arm and shadow band.

could 1) find more motion vectors near edges and 2) relieve the boundary effects (Figure 4).

C. Filling

We adopt two different approaches to fill in the missing information. The first approach is “local mean-filling” in which the missing area will be filled with the local mean value of adjacent neighboring areas. It removes the majority of the spurious motion vectors that are near to the holding arm and shadow band.

The second approach is to fill in the missing information with the estimated cloud. Once we fill the information, we can obtain better motion vector quality. Figure 5 shows before and after filling in missing information area and in the latter we

could find more accurate motion vectors.

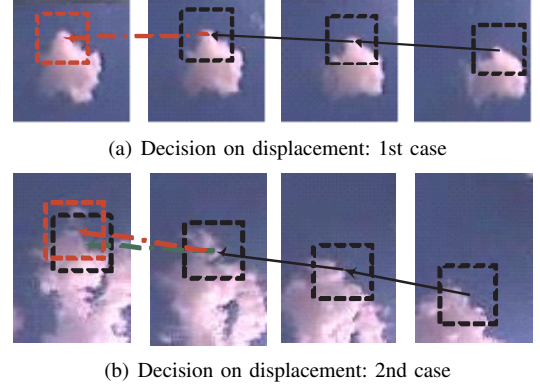


Fig. 6. Motion Vector Back-tracking

D. Sequential Motion Vector Prediction

To cope with the abnormal motion vectors due to cloud shape changes (which hasn’t been considered in the existing paper [26]), we propose a motion vector estimator to improve the accuracy and stability of cloud motion vectors. We try to predict next g ($g \geq 1$) frame motion vectors from h preceding frames. Since it utilizes h recent frames, it is much more stable and robust compared to the prediction using only two recent frames. The motion vector prediction consists of three components: 1) back-tracing the same block from the current frame back to $h + 1$ preceding image frames, 2) using a series of recent motion vector trends to build a sequential prediction model, and 3) predicting future motion vectors from the sequential model.

Figure 6 shows the first step and back-tracking. We back-trace a block starting at (i, j) of the current image frame I^t back to the previous frame I^{t-1} and we could repeat this process until $h + 1$ previous frames are checked. To increase the stability of our back-tracking step, we compare the detected back-traced motion vector with the predicted one. If the Euclidean distance between these two is larger than a threshold b , the predicted motion vector is chosen as the final motion vector (Figure 6(a)), otherwise, the detected motion vector is chosen (Figure 6(b)) to allow local motion vector digression resulted from smooth cloud shape changes. Iteratively using the same method on $h + 1$ frames, we can find h motion vectors namely from $\vec{v}_{(i,j)}^{t-h}$ to $\vec{v}_{(i,j)}^t$ for the same block (i, j) . Note that the block index (i, j) is the same for all h historical motion vectors because we do back-trace from the current block index (i, j) of current time t . For this process, we use fast cross correlation (Section IV). In the rest of this

paper, we use \vec{v}^t instead of $\vec{v}_{(i,j)}^t$ for the notational simplicity whenever it is easy to distinguish.

The second step is to learn linear prediction models.

$$\hat{\vec{v}}^{t+1} = \sum_{k=1}^h \vec{w}_k \cdot \vec{v}^{t-h+k} \quad (2)$$

where $\hat{\vec{v}}^{t+1}$ is the predicted motion vector, \vec{v}^{t-h+k} are the previous observed motion vectors, and \vec{w}_k are the coefficients of the previous motion vectors. Our goal is to minimize the following loss function:

$$\operatorname{argmin}_W \left\{ \sum_{t=h}^{n-1} \left(\sum_{k=1}^h \vec{w}_k \cdot \vec{v}^{t-h+k} - \vec{v}^{t+1} \right)^2 + \lambda \sum_{k=1}^h \vec{w}_k \cdot \vec{w}_k' \right\} \quad (3)$$

where n is the number of training image frames and λ is a regularization parameter.

To predict next g motion vectors, we sequentially predict from \vec{v}^{t+1} to $\hat{\vec{v}}^{t+g}$ using the following equation.

$$\hat{\vec{v}}^{t+g} = \sum_{k=1}^{h-g-1} \vec{w}_k \cdot \vec{v}^{t-h+k} + \sum_{k=h-g}^{h-1} \vec{w}_k \cdot \hat{\vec{v}}^{t-h+k} \quad (4)$$

E. Wind-Field Extraction

Algorithm 1: Windfield-Extraction(V , th_{cos} , lth_{ratio} , uth_{ratio})

Input: V is a motion vector matrix, th_{cos} is similarity threshold, lth_{ratio} and uth_{ratio} are the lower and upper bound norm length ratio thresholds

Output: Wind-field WF

```

1 Let  $\vec{v}_i$  be the  $i^{th}$  largest number of motion vectors in  $V$ 
  ( $\vec{v}_1, \dots, \vec{v}_m$ );
2 foreach  $\vec{v}_i$  from  $\vec{v}_1$  to  $\vec{v}_m$  do
3   if  $WF = \emptyset$  then
4     Add  $\vec{v}_i$  to  $WF$ ;
5     continue to step 2;
6   end
7   foreach  $\vec{v}_j \in WF$  do
8      $sim = \cos(\vec{v}_i, \vec{v}_j)$ ;
9      $ratio = ||\vec{v}_i||_2 / ||\vec{v}_j||_2$ ;
10    if  $sim \geq th_{cos}$  and  $lth_{ratio} \leq ratio \leq uth_{ratio}$ 
11      then
12        continue to step 2;
13    end
14  if the number of  $\vec{v}_i \geq 2\%$  of the number of
    non-empty motion vectors then
15    Add  $\vec{v}_i$  to  $WF$ ;
16  end
17 end

```

Wind-field is three-dimensional spatial patterns of winds with uniform/similar wind speeds (Figure 7). There are two advantages in using wind-field in our prediction model. First,

we would like to use the spatial patterns of winds or motion vectors to identify and remove spurious motion vectors. Second, we can only observe the lowest layer of cloud with TSI imager if there exist multiple layers of cloud. Hence it is especially important to extract wind-field patterns, and use them to estimate the motion vectors of the multi-layer cloud.

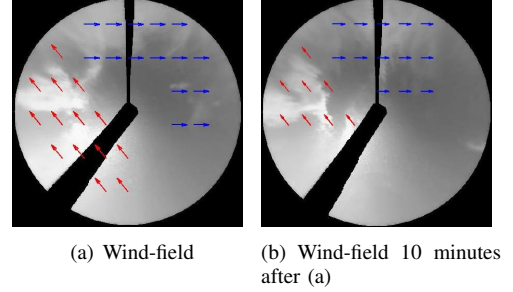


Fig. 7. Two wind-field extraction from motion vector statistics, one wind-field direction as red arrows, the other one as blue arrows

Our wind-field extraction algorithm relies on three key characteristics of wind-field: frequency of motion vector, cosine similarity and motion vector length similarity. Algorithm 1 describes various wind-field extraction procedures. Algorithm 2 explains how to adjust motion vectors using local and global wind-field. Here local wind-field is extracted from the motion vectors within a local neighborhood in a single time frame, while global wind-field is extracted from all motion vectors at a given time t .

VI. CLOUD MOTION ESTIMATION

Two approaches to estimate and predict upcoming sky images are provided in this section. The first one is for single layer cloud, and the second is for multi-layer cloud based on wind-field pattern.

A. Single Layer Estimation

The core idea of estimating the new cloud image for a future time frame is to use the motion vectors described in Section V to project the latest frame (t) into a new frame ($t+g$) where $g \geq 1$. Here we make an assumption that the cloud will only change its shape smoothly and maintain a constant velocity in a short time period [25].

As we used image sub-blocks to detect motion vectors, cloud motion estimation is simplified to estimate block-wise movements where each block starting at (i, j) on time t with block size $m \times m$ ($I_{(i,j)(i+m-1,j+m-1)}^t$) has one motion vector $\vec{v}_{(i,j)}^t = \langle u, v \rangle$ where I^t is the image frame at time t .

$$I_{(i+u,j+v)(i+u+m-1,j+v+m-1)}^{t+1} = I_{(i,j)(i+m-1,j+m-1)}^t \quad (5)$$

However, Equation 5 will generate mosaic effects between block boundaries. To remove this type of mosaic effects and improve the estimated image quality, we also apply the following four methods: 1) we enlarge the moving block size by adding borders around it, 2) if some blocks are projected to overlap at the estimated time frame, then we calculate the mean value of them as the final image values, which can

Algorithm 2: MotionVector-Adjustment(V , th_{cos} , lth_{ratio} , uth_{ratio})

Output: Adjusted motion vector matrix V'

```

1  $GWF = \text{Windfield-Extraction}(V, th_{cos}, lth_{ratio}, uth_{ratio});$ 
2 foreach  $\vec{v}_{(i,j)}$  of  $V$  do
3   Let  $LV$  be the local neighborhood motion vectors of  $\vec{v}_{(i,j)}$ ;
4    $LWF = \text{Windfield-Extraction}(LV, th_{cos}, lth_{ratio}, uth_{ratio});$ 
5   Let  $v_{hf}$  be the highest frequency windfield;
6   foreach  $\vec{v}_{wf}$  of  $GWF$  do
7      $sim = \cos(\vec{v}_{wf}, \vec{v}_{hf})$ ;
8      $ratio = ||\vec{v}_{wf}||_2 / ||\vec{v}_{hf}||_2$ ;
9     if  $sim \geq th_{cos}$  and  $lth_{ratio} \leq ratio \leq uth_{ratio}$  then
10       $\vec{v}_{(i,j)}^t$  of  $V' = \vec{v}_{hf}$ ;
11      continue to step 2;
12   end
13 end
14 end

```

smooth the boundary effect of a block and get a better version of the estimated image, 3) if the moving block contains no sky images (e.g. the blocks overlap with shadowband, camera-holding arm, and the area outside the TSI circle), we only process (move) the fraction of the block with image data, and 4) for the blank area within an image block, we fill it with the default clear sky texture, and move it based on the motion vector as well.

B. Multi Layer Estimation

Given the wind field in multiple history frames, we can determine the order of wind field in terms of altitude, which is extremely important, but not considered in [26]. For every frame we obtain the enclosed areas of different cloud layer (each with different wind field). With the current wind field speed, we can detect whether there will be any area with overlapping cloud layers (suppose g minutes later). Once we get the real frame for g minutes later, we examine the same area to validate the estimation result. Suppose there are two cloud layers, A and B , the current detected wind field for this area, A , would have much lower altitude than B . For every ten minutes the program re-examine the wind field order in terms of altitude. During estimation, we only keep the lowest cloud texture in the future overlapped area of estimated frame, which is different from the single layer cloud estimation.

VII. SOLAR IRRADIANCE PREDICTION

In this section, we provide a linear prediction model for real-time solar irradiance forecasting based the cloud motion estimation and tracking developed in the previous sections. The real time solar irradiance monitoring data, along with TSI images with the predicted cloud information from prior steps

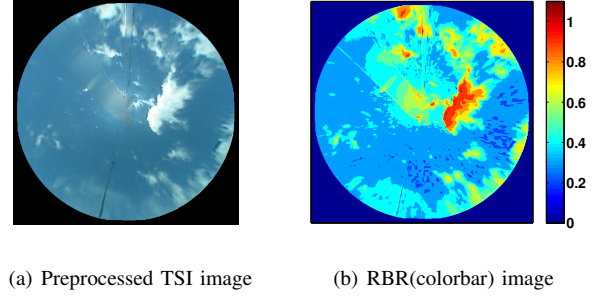


Fig. 8. RBR conversion of TSI image

are used for our model input. The model will output solar irradiance values as the prediction result which can be used to straightforwardly estimate the energy production from the photovoltaic array. The power output estimation from a particular solar farm configuration is also determined by various factors (panel manufacturer, orientation, surface temperature), and not in the scope of this paper.

By its design, a 2D TSI imager captures a huge amount of information about the sky regions within the TSI optical range. After the preprocessing step which removes the image distortion, the image area inside a cone of 60 degrees has practically a sufficient pixel resolution for extracting the cloud related data. It is expected that when the cloud passes the sun location in the sky, the ground radiation reading experiences a deduction in sync with the cloud's motion. The amount of the decrease depends on many factors ranging from the cloud's size, thickness, chemical compositions to the ambient environment's physical conditions. The main simplification in our model is to replace all these complex and intercorrelated data with a few empirically extracted parameters. Even our model might potentially oversimplify the factors of solar irradiance, our later analysis shows that the model nonetheless performs reasonably well and is even superior to those models relying heavily on external climate data provided by solar site's nearby weather stations.

These observations motivates our TSI image based approach to the modeling and forecasting of cloud conditions, it also consolidates our intuitive picture that due to the real-time nature of our forecasting, the ambient climate conditions plays a relatively insignificant role compared to the much more volatile microscopical changes in the sun's direct optical path. In effect, we find that among these pixels, only a small cluster within a few hundreds pixel sizes of the sun's position on the TSI image has significant correlations with our pyranometer readings fluctuations. This cluster's exact size is up to choice and we perform an optimization with respect to this size in our data analysis.

To explain the main concept with our model, we consider the following simple model for the correlation between the TSI image and solar irradiance values. Both data streams are treated as discrete time series, namely $Rad(t)$ and $RBR(t)$, each of which is sampled at two different step sizes: respectively one- and two- minute intervals. In the linear prediction

model used by our paper, the value at one time step depends only on the immediate preceding time step:

$$\text{Rad}(t) = \text{Rad}(t-1) + C \times (\text{RBR}(t) - \text{RBR}(t-1)) \quad (6)$$

Here $\text{Rad}(t)$ is the time series of pyranometer radiation readings in W/m^2 , and $(\text{RBR}(t) - \text{RBR}(t-1))$ defines a time series of the TSI image red-blue ratio (RBR) value change w.r.t the prior step. The TSI image is a 2D integer matrix whose elements are in the range in $[0, 255]$. The derived red-blue ratio is a continuous real number. Hence both time series used in this paper have indeed real value. Our choice to use RBR as an indicator of clouds is validated by the finding that RBR consistently differentiates clear sky v.s. different levels of cloudy sky.

The coefficient C in our equation (6) defines the correlation between cloud and radiation. It is obvious that the correlation between the RBR value and the pyranometer radiation readings is negative. In fact, based on statistical analysis of a vast number (about thirty thousands) of local TSI images with varying cloud distributions, we found that the RBR value of cloud pixels consistently fall into the neighborhood between 0.6 and 1 (see figure 8), while theoretically this range could have been much bigger. A similar threshold (termed as Sunshine Parameter) is made of essential use in [26] for binary characterization of cloudy and clear sky conditions. In our approach, this observation helps to validate that our experiments correctly extract a negative value for the parameter C , we make no essential use of the precise value as threshold to distinguish clouds from clear backgrounds.

VIII. EXPERIMENTS

A. Data Selection and Preprocessing

In the experiments we use mature TSI image and irradiation data from Atmospheric Radiation Measurement (ARM) Climate Research Facility [14]. We select two typical ARM site with remarkably different weather to test our cloud motion estimation. The data diverseness can show the feasibility of our cloud motion detection and estimation algorithms. In the Arm site located at Southern Great Plains Central Facility, Ponca City, Oklahoma (SGP), Class 4 wind resource is prevalent almost over all year. The wind direction of the SGP is fairly constant from the south or southwest, and the wind speed has a small diurnal variation except nighttime or early morning [27]. The cloud motion during daylight time under such weather is slow and change smoothly. Therefore the cloud motion estimation has a supreme preference on a slightly longer term (up to 10 minutes). In the Arm site located at Tropical Western Pacific Darwin Site, Northern Territory, Australia (TWP), the wind speed and direction is always in dramatical change due to the typical tropical weather [28]. Therefore the cloud motion in TWP site is very variable and the life of cloud is usually shorter than some other ARM sites.

Our experiments use four days data from SGP, and two days data from TWP collected by the DOE (Department of Energy) ARM program [14]. In the experiments, we only pay attention to the cloud motion estimation from 3 hours before to

3 hours after the local solar culmination time (720 TSI images in 6 hours with every 30 seconds per frame). During this time period, the cloud coverage has higher correlation with actual solar energy production. To show the accuracy and robustness of our proposed method, we choose six days worth of data with a wide variety of cloud conditions. June 27th 2010 from SGP and September 11th 2010 from TWP have high cloud coverage, and radically shape-changing cloud with multiple layers. Such type of clouds are in general hard to estimate; July 12th 2010 from SGP shows single layer cloud but with high sky coverage and mild cloud shape changes; August 6th 2010 from SGP show multi-layer cloud with motion direction that changes smoothly; October 25th 2010 from TWP although has low cloud coverage, has radically shape-changing cloud with multiple layers, and August 16th 2010 from SGP has scattered single layer cloud. We did not consider sunny or rainy days because it is straightforward to predict the solar radiation level during these days. The diverse data selected is intended to study the robustness of our cloud motion detection and estimation algorithms.

Five preprocessing steps are applied before cloud motion vector detection and estimation: 1) convert the input image format to grayscale; 2) scale the intensities of the input image to the full 8-bit intensity range $[0, 255]$; 3) correct the barrel distortion from camera; 4) undistort the image to a normal format (Figure 2); and 5) remove the shadowband and camera holding arm of TSI image (in our methods we use algorithm in [11] to detect the sun position and set such area as black).

B. Motion Estimation Parameters

For fast cross correlation method, there are three parameters: 1) block size, 2) block overlapping size and 3) search window size. In theory, the block size should be kept large enough to ensure stable results but it should not be too big to capture accurate and enough motion vectors. The size of the search window must be sufficiently larger than the expected displacement but too large search window increases the chance to capture spurious motion vector as well. To adapt the motion detection algorithm in TSI circular shape image, we use two block sizes, the bigger block size for the center part and the smaller block size for pixels close to circle edge of an TSI image. With the proposed two block sizes, we could 1) obtain more number of accurate motion vectors near edges and 2) relieve the boundary effects. In our experimental comparison, we use the same parameters as in [6].

C. EMD Evaluation

In the following experiment, we use the most recent frame as our baseline (BL) approach. We compare motion estimation using only two frames ($2F$) which is equal or better than [26] due to refined gap filling, multi frames using sequential motion vector prediction (MF) and multi frames with wind field adjustment ($MF + WF$). Our proposed three approaches include two block sizes, local-mean filling, and the estimated image filling. Since we have the ground truth of TSI images

TABLE I
PROPERTIES OF SELECTED DATES

Date	Location	The number of images	Layers	Coverage	Shape Changes
6/27/2010	SGP	720	multi	high	radical
9/11/2010	TWP	720	multi	high	radical
7/12/2010	SGP	720	single	high	medium
8/06/2010	SGP	720	multi	low	mild
10/25/2010	TWP	720	multi	low	radical
8/16/2010	SGP	720	single	low	mild

for each estimation, we compare our estimated results to the true TSI images.

Especially, earth mover's distance (EMD) was used as our only evaluation metric because EMD has very nice properties on revealing image similarity. EMD allows for partial matches in a very natural way which is of importance to deal with image occlusions and clutter. Consequently, in TSI cloud image comparison, EMD matches perceptual similarity better than other measures. In [22], computing of EMD can be formalized as a linear programming problem as follows: denote the first image with m rows as $P = (p_1, w_{p_1}), \dots, (p_m, w_{p_m})$, where p_i is the row representative and w_{p_i} is the weight of the row; the second image $Q = (q_1, w_{q_1}), \dots, (q_n, w_{q_n})$ is denoted similarly. $\mathbf{D} = [d_{ij}]$ is the ground distance matrix where d_{ij} is the ground distance between rows p_i and q_j . EMD tends to find a flow $\mathbf{F} = [f_{ij}]$, with f_{ij} the flow between p_i and q_j , that minimizes the overall cost

$$\text{WORK}(P, Q, \mathbf{F}) = \sum_{i=1}^m \sum_{j=1}^n f_{ij} d_{ij},$$

subject to the following constraints:

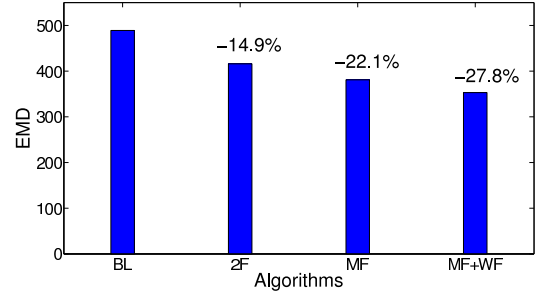
$$\begin{aligned} f_{ij} &\geq 0 & 1 \leq i \leq m, 1 \leq j \leq n \\ \sum_{j=1}^n f_{ij} &\leq w_{p_i} & 1 \leq i \leq m \\ \sum_{i=1}^m f_{ij} &\leq w_{q_j} & 1 \leq j \leq n \\ \sum_{i=1}^m \sum_{j=1}^n f_{ij} &= \min\left(\sum_{i=1}^m w_{p_i}, \sum_{j=1}^n w_{q_j}\right), \end{aligned}$$

According to the analysis in [22], the first constraint allows moving "supplies" from P to Q and not vice versa. The next two constraints limit the amount of supplies that can be sent by the rows in P to their weights, and the rows in Q to receive no more supplies than their weights; and the last constraint forces to move the maximum amount of supplies possible. This amount is called the total flow. Once the transportation problem is solved, and we have found the optimal flow \mathbf{F} , the earth mover's distance is defined as the work normalized by the total flow:

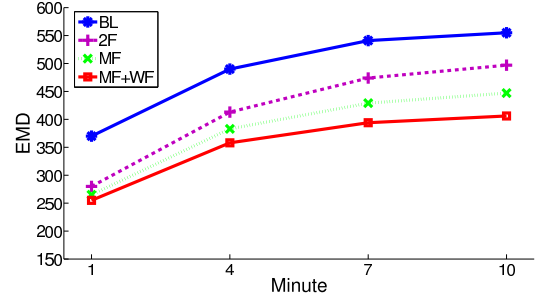
$$\text{EMD}(P, Q) = \frac{\sum_{i=1}^m \sum_{j=1}^n f_{ij} d_{ij}}{\sum_{i=1}^m \sum_{j=1}^n f_{ij}}.$$

where normalization factor is introduced in order to avoid favoring smaller signatures in the case of partial matching.

During experiments, we shrink all the images to 120×120 pixels in order to fit the system memory capability. Figure 11 shows one case of EMD comparison result between four methods.



(a) Overall Average



(b) Averages for Different Prediction Span

Fig. 9. Comparison of four algorithms on four different days from SGP

D. Motion Estimation Results

The cloud motion on SGP site are very slow and smooth, therefore our estimation experiments on SGP are tested on 1, 4, 7 and up to 10 minutes prediction. Comparably, TWP has very dramatically changing cloud and the life of cloud is much shorter due to the typically tropical weather, hence we only test on 0.5, 1 and up to 2 minutes cloud estimation.

Motion estimation results on SGP are shown in Figure 9 for overall evaluation and Figure 10 for each different days. In Figure 9(b) the horizontal axis denotes our four prediction time choices, 1, 4, 7 and up to 10 minutes; the vertical axis denotes the corresponding Earth Mover's Distance (EMD). The following is our summary of analysis on SGP experiments:

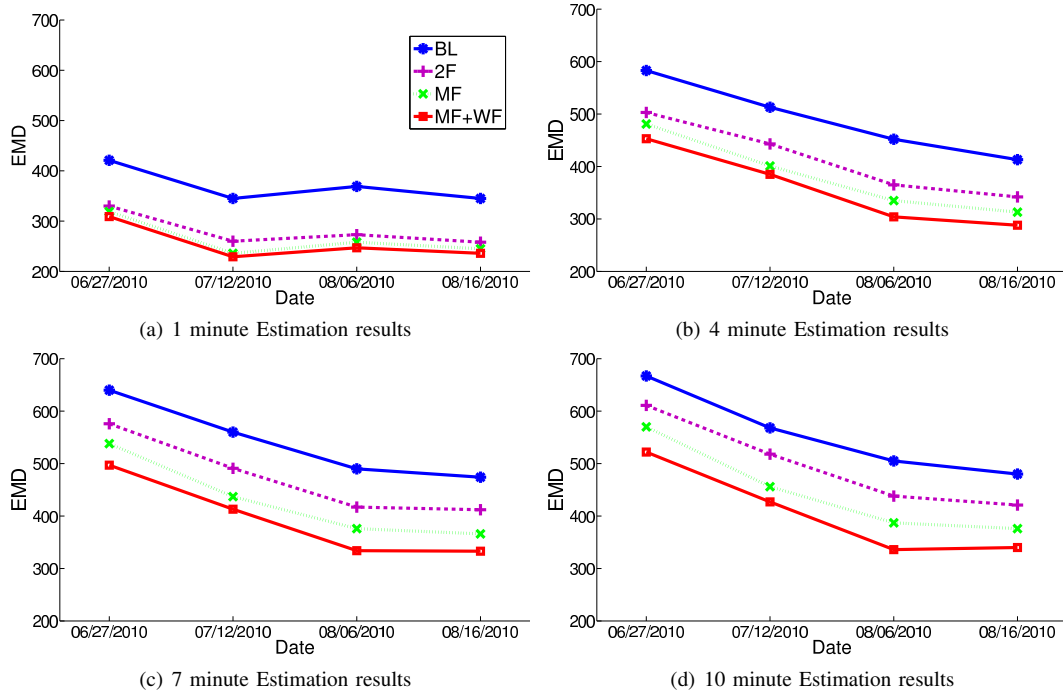


Fig. 10. Comparison of four algorithms on four different days from SGP

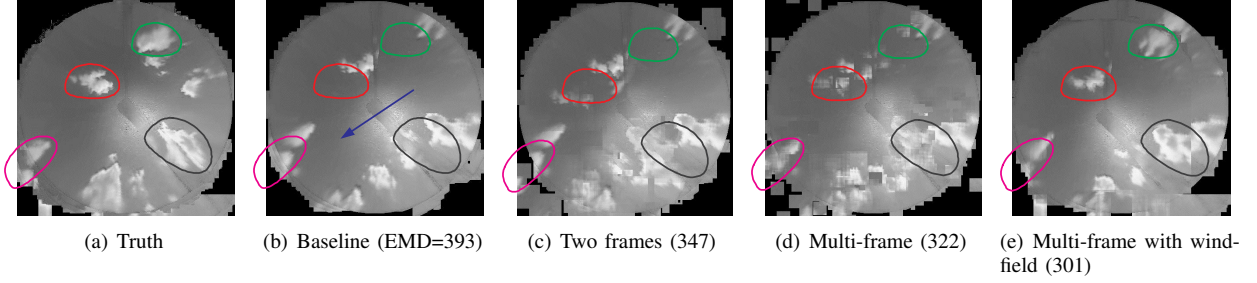


Fig. 11. Case study: Four minute prediction on Aug 6, 2010 from SGP. The numbers are earth mover's distance compared to the ground truth.

- 1) Overall our proposed approaches significantly improve the cloud motion estimation quality from 14.9% to 27.8% (Figure 9(a)). $2F$ shows the minimum 14.9% improvement and $ML + WF$ shows the best 27.8% improvement over baseline.
- 2) As we increase the prediction span from one minute to ten minutes, our sophisticated MF and $MF + WF$ models show much better performance than $2F$ (Figure 9(b)). On one minute estimation, any prediction model show quite similar results but $MF + WF$ show the best average performance on ten minute prediction.
- 3) When the cloud shape radically changes and there are multi-layer clouds (June 27 2010), all four methods are suffering compared to the other three cloud types in SGP (Figure 10). However, the improvement we observed is consistent across all four days of SGP.
- 4) When there are multi-layer clouds (June 27 2010 and Aug 6 2010), $MF + WF$ shows more improvements over MF which is more obvious on 7 and 10 minutes prediction.
- 5) The mild scattered clouds (Aug 6 2010 and Aug 16 2010)

are easier to predict than high cloud coverage (July 12 2010), which is good news for solar panel power output prediction.

We provide a case study to illustrate cloud motion estimation results and their earth mover's distance relations (Figure 11). We trace four circled clouds from the truth (Figure 11(a)) except the upper right cloud which didn't appear on baseline. As expected, the baseline could not track clouds well. $2F$ captured part of red and black circles but failed to track green and purple circles. MF improved four circles over $2f$ but it only traced partially (red and green) and the traced cloud is not clear (purple and black). Our most advanced method $MF + WF$ successfully captured all four clouds with clear shape. So EMD of $MF + WF$ is minimal although estimated cloud shape is not exactly the same to the truth.

For TWP cloud estimation, we also run $2F$, MF and $MF + WF$ experiments on the two selected days: September 11th 2010 and October 25th 2010. In Figure 12 the horizontal axis denotes our four prediction time choices, 0.5, 1, and up to 2 minutes; the vertical axis denotes the corresponding Earth

Mover's Distance (EMD). The result, once again, confirms that our $MF + WF$ outperforms not only BL with 46.59%, but also the existing typical cloud motion estimate using $2F$. Although the $MF + WF$ only slightly improves based on MF less than 4%. The reason is because of the dramatically changing wind-field in TWP site.

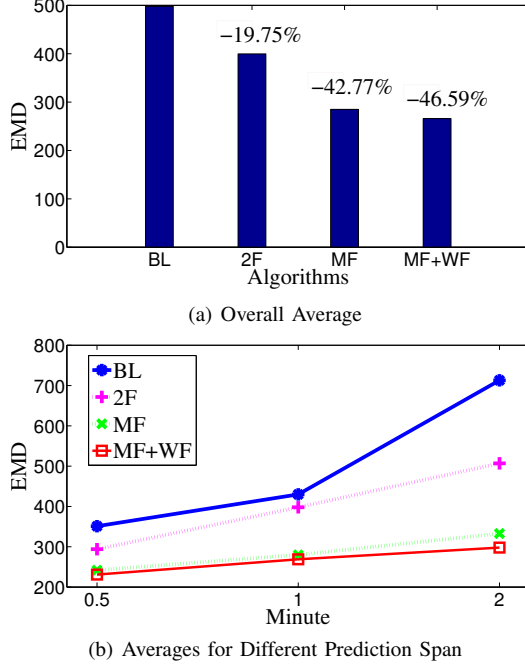


Fig. 12. Comparison of four algorithms on two different days from TWP

E. Solar Irradiance Prediction

In this section we used the TSI images taken on September 11, 2010 at TWP for testing of our model. We made two predictions, 1 minute and 2 minutes respectively, with our linear prediction model (LP). One advantage of our algorithm is that it can generate the desired outputs of different prediction time ranges without modifying input data. We used the binary model in [26] as a baseline for comparison, and set its time step to be 1 minute.

From the TSI's geographical location and date, we can accurately calculate Sun's position on the original TSI image. Then we use the coordinate transformation in the preprocessing algorithm to map Sun's position into the corresponding pixel in the undistorted TSI image.

Around this pixel, we choose various window sizes for the surrounding pixel block ranging from 10×10 to 50×50 pixel. Experiments confirmed that a window of such sizes entails the information with a strong correlation to the pyranometer reading changes, while at the same time can avoid the random errors of the motion estimation algorithm. Among our analysis findings, the window size of 20×20 pixel is consistently optimal, and therefore selected for subsequent analysis of our model.

The sample from TWP local time 10:00 to 16:00 hours contains 360 TSI images with the matching solar irradiance

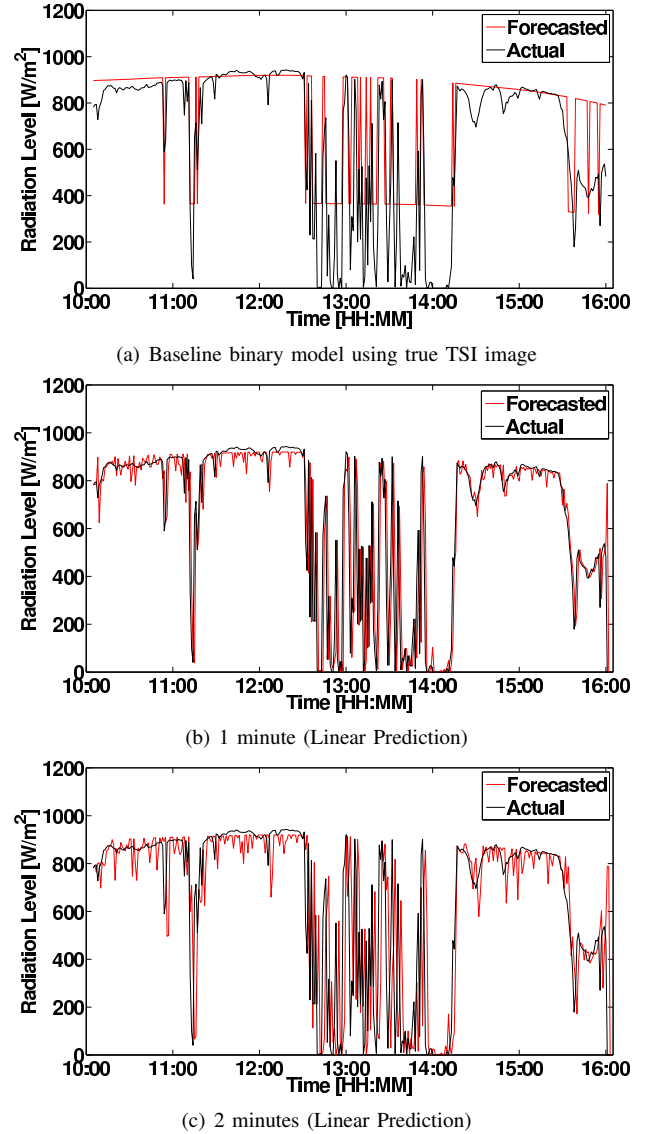


Fig. 13. Comparisons of our radiation prediction models with UCSD binary model

readings taken once per minute. We use them as the input data streams for the model (6). In addition we setup an upper bound curve for the predicted solar irradiance values. The upper bound changes along with the time during course of six hours. For the experiment, we chose the values from the radiance curve of TWP on September 17, 2010 when it was a perfect clear sky all day long. The effect on the predicted real-time irradiance value curve can be seen from the plateaus in plots (a) and (b) of figure (13). Nevertheless, in the binary model [26] a lower bound of 40% of GHI value was imposed. Consequently, the model produced noticeable deviations from actual pyranometer radiation readings on the randomly selected day.

We used 10-fold cross validation for our linear prediction model based on the TWP sample. We did not obtain the executable of the baseline binary method. Therefore we had to

skip their cloud motion estimation step, and fed the competing baseline model directly with the ground truth, i.e. the actual TSI cloud image of the next time step. The output of this baseline is actually generated directly by filtering the real TSI data with their threshold method prescribed in [26]. Two thresholds used in the baseline model are called GHI and SP. The RMSE scores of the baseline model under this treatment is much better than that of the actual step-by-step execution. The respective RMSE results are given in Table II.

TABLE II
RMSE RESULTS COMPARISON

UCSD binary baseline	1 min LP	2 min LP
206.85	142.08	177.72

The [26] baseline as explained above is not a real prediction and hence we need not perform cross validation on it. The comparison is then biased towards the binary method, as it also has no propagated error from the motion estimation algorithm. Nevertheless, the advantage of our model is validated by a smaller (better) RMSE value.

Our testings also confirmed a negative correlation between the RBR value within the solar window and the solar irradiance value. The experimental values range between $C = -46.08$ and -69.74 for the 10-fold cross validations for the 1-minute and 2-minute forecasts.

IX. CONCLUSION

We introduced cloud motion estimation algorithms for short term solar radiation level predictions and addressed special challenges and requirements associated with cloud prediction using TSI images and pyranometer solar irradiance readings. In particular, we adopted fast cross correlation method to satisfy the real-time processing requirement and improve accuracy in detection of cloud motion vectors. Two novel approaches were used to handle the uniqueness of TSI images: 1) using two different block sizes for motion vector detections, and 2) filling the gap with a local mean for estimated images. Furthermore, we implemented a sequential motion vector prediction algorithm to deal with cloud shape changes, and proposed wind-field detection and motion vector adjustment algorithms to handle multi-layer clouds. Finally, we provided a prediction pipeline of integrating these algorithms and methods to process the workflow from the image preprocessing step to the final cloud motion estimation and solar irradiance forecast at the 1-2 minute scale. The experiments demonstrated that our approach significantly outperforms the baseline estimation with 28% improvement on average consistently. Furthermore, we expect that our future development implementing multiple TSI devices will both greatly expand the length of the prediction time window and improve the quality of our motion estimation and solar irradiance predictions.

REFERENCES

[1] J. Magarey and N. Kingsbury *Motion Estimation using a Complex-valued Wavelet Transform*, IEEE Transactions on Signal Processing, 46(4), 1069–1084, 1998.

[2] A. Arking and R. C. Lo and A. Rosenfeld *A Fourier Approach to Cloud Motion Estimation*, Journal of Applied Meteorology, 735–744, 1977.

[3] S. S. Beauchemin and J. L. Barron *The Computation of Optical Flow*, ACM Computing Surveys (CSUR) Surveys 27(3), Sept. 1995.

[4] J. Marcello and F. Eugenio and F. Marques, *Cloud Motion Estimation in Seviir Image Sequences*, IEEE IGARS, 2009.

[5] P. Heas and E. Memin, *Three-Dimensional Motion Estimation of Atmospheric Layers From Image Sequences*, IEEE Transactions on Geoscience and Remote Sensing, 46(8), 2385–2396, AUGUST 2008.

[6] H. Huang and S. Yoo and D. Yu and D. Huang and H. Qin, *Cloud Motion Detection for Short Term Solar Power Prediction*, ICML 2011 Workshop on Machine Learning for Global Challenges.

[7] D. I. Barnea and H. F. Silverman, *A class of algorithms for fast digital image registration*, IEEE Trans. Computers, 21, 179–186, 1972.

[8] M. Kass, A. Witkin and D. Terzopoulos, *Snakes: Active contour models*, Proc. 1st Int. Conf. on Computer Vision, 259–268, 1987.

[9] A. R. Lindsey, *The Non-Existence of a Wavelet Function Admitting a Wavelet Transform Convolution Theorem of the Fourier Type*, Rome Laboratory, 1995.

[10] D. Decarlo and D. Metaxas, *Deformable Model Based Face Shape and Motion Estimation*, Proc. International Conf. Face and Gesture Recognition, 1996.

[11] I. Reda and A. Andreas, A. *Solar position algorithm for solar radiation application*, National Renewable Energy Laboratory (NREL) Technical report NREL/TP-560-34302, 2003.

[12] T. Chanwimaluang, G. Fan, and S. R. Fransen, *Hybrid retinal image registration*, IEEE Trans. Info. Tech. Biomed., 10(1), 129–142, 2006.

[13] P. Glomb, *Detection of interest points on 3D data: Extending the harris operator*, In Computer Recognition Systems 3, vol. 57 of Advances in Soft Computing. Springer Berlin / Heidelberg, 103–111, 2009.

[14] *TSI Images 2010*, <http://www.arm.gov/instruments/tsi>, Atmospheric Radiation Measurement (ARM) Climate Research Facility, 2010.

[15] P. Anandan, *A computational framework and an algorithm for the measurement of visual motion*, Int. J. Computer Vision 2(3), 283–310, 1989.

[16] P. J. Burt, C. Yen, X. Xu, *Local correlation measures for motion analysis: a comparative study*, IEEE Conf. Pattern Recognition Image Processing, 269–274, 1982.

[17] T. W. Ryan, *The prediction of cross-correlation accuracy in digital stereo-pair images*, 1981.

[18] J. P. Lewis, *Fast normalized cross-correlation*, Vision Interface, 1995.

[19] T. J. Greenwald, R. Hertenstein, T. Vukicevic, *An all-weather observational operator for radiance data assimilation with mesoscale forecast Models*, Mon. Wea. Rev., 130, 1882–1897, 2002.

[20] T. Vukicevic, T. Greenwald, M. Zupanski, D. Zupanski, T. Vonder Haar, A. S. Jones, *Mesoscale cloud state estimation from visible and infrared satellite radiances*, Monthly Weather Review. 132(12), 3066–3077. Dec. 2004.

[21] R. L. Fogt, D. H. Bromwich, *Atmospheric moisture and cloud cover characteristics forecast by AMPS*, Wea. Forecasting, 23, 914–930. 2008.

[22] Y. Rubner, C. Tomasi, L. J. Guibas, *The earth mover's distance as a metric for image retrieval*, International Journal of Computer Vision 40(2), 99–121, 2000.

[23] T. Brox, A. Bruhn, N. Papenberg, J. Weickert, *High accuracy optical flow estimation based on a theory for warping*, Computer Vision-ECCV, 3024, 25–36, 2004.

[24] T. Brox, J. Malik, *Large displacement optical flow: descriptor matching in variational motion estimation*, IEEE Transactions on Pattern Analysis and Machine Intelligence, 33(3), 500–513, Mar. 2011.

[25] R. R. Rogers, *A short course in cloud physics, 2nd Edition*, Pergamon Press, Oxford, England, 235 pp, 1979.

[26] C. W. Chowa, B. Urquhart, M. Lavea, A. Dominguez, J. Kleissla, J. Shieldsb and B. Washomc, *Intra-hour forecasting with a total sky imager at the UC San Diego solar energy testbed*, Solar Energy, 85(11), 2881–2893, 2011.

[27] S. Zhong, J. D. Fast, and X. Bian, *A Case Study of the Great Plains Low-Level Jet Using Wind Profiler Network Data and a High-Resolution Mesoscale Model*, Monthly Weather Review, 124, 785–806, 1996.

[28] C. Zhang, *Atmospheric Intraseasonal Variability at the Surface in the Tropical Western Pacific Ocean*, Journal of Atmospheric Sciences, 53(5), 739–758, 1996.